Comput. Methods Appl. Mech. Engrg. 197 (2008) 4160–4172

Contents lists available at ScienceDirect

Comput. Methods Appl. Mech. Engrg.

journal homepage: www.elsevier.com/locate/cma

Three-dimensional viscous finite element formulation for acoustic fluid–structure interaction

Lei Cheng [a,*], Robert D. White [b], Karl Grosh [c]

[a] Department of Mechanical Engineering, 2350 Hayward Avenue, University of Michigan, Ann Arbor, MI 48109-2125, USA
[b] Department of Mechanical Engineering, 200 College Avenue, Tufts University, Medford, MA 02155, USA
[c] Department of Mechanical and Biomedical Engineering, 2350 Hayward Avenue, University of Michigan, Ann Arbor, MI 48109-2125, USA

ARTICLE INFO

Article history:
Received 18 December 2007
Received in revised form 4 April 2008
Accepted 13 April 2008
Available online 25 April 2008

Keywords:
Viscous
Finite element formulation
Acoustic fluid–structure interaction

ABSTRACT

A three-dimensional viscous finite element model is presented in this paper for the analysis of the acoustic fluid–structure interaction systems including, but not limited to, the cochlear-based transducers. The model consists of a three-dimensional viscous acoustic fluid medium interacting with a two-dimensional flat structure domain. The fluid field is governed by the linearized Navier–Stokes equation with the fluid displacements and the pressure chosen as independent variables. The mixed displacement/pressure based formulation is used in the fluid field in order to alleviate the locking in the nearly incompressible fluid. The structure is modeled as a Mindlin plate with or without residual stress. The Hinton–Huang's 9-noded Lagrangian plate element is chosen in order to be compatible with 27/4 u/p fluid elements. The results from the full 3D FEM model are in good agreement with experimental results and other FEM results including Beltman's thin film viscoacoustic element [W.M. Beltman, P.J.M. Van der Hoogt, R.M.E.J. Spiering, H. Tijdeman, Implementation and experimental validation of a new viscothermal acoustic finite element for acousto-elastic problems, J. Sound Vib. 216 (1) (1998) 159–185] and two and half dimensional inviscid elements [A.A. Parthasarathi, K. Grosh, A.L. Nuttall, Three-dimensional numerical modeling for global cochlear dynamics, J. Acoust. Soc. Am. 107 (2000) 474–485]. Although it is computationally expensive, it provides a benchmark solution for other numerical models or approximations to compare to besides experiments and it is capable of modeling any irregular geometries and material properties while other numerical models may not be applicable.

Published by Elsevier B.V.

1. Introduction

This paper deals with numerical modeling of three-dimensional fluid–structure interaction problems using the finite element method (FEM). Modeling fluid–structure interaction involves the analysis of the fluid domain, the structure domain and the coupling between these two domains. While the structure domain is generally described in a displacement formulation, there are a number of FEM formulations available for modeling the fluid field depending on the properties of the fluid. The fluid can usually be categorized into two different groups: the fluid flow and the acoustic fluid with small particle motions. For a general fluid flow problem, a full Navier–Stokes equation is required to model the fluid field, while for the acoustic fluid, the fluid is often assumed to be linear and inviscid so that the fluid formulation can be greatly simplified. However, in a wide range of structural acoustic problems, the viscous effect plays an important role, especially in the system with a thin fluid layer such as the trapped fluid hydromechanical cochlear model [25]. In these circumstances, the fluid viscosity is non-negligible and should be included in the acoustic fluid model. In this paper, we aim at developing a three-dimensional FEM formulation for the analysis of the viscous acoustic fluid coupled with a flexible boundary.

The commonly used fluid formulations include the pressure formulation [21], the potential formulation [7,18], the displacement formulation [15,11] and the combination of some of them [23,1]. Choosing a scalar variable such as pressure for the fluid field significantly reduces the problem size compared to the displacement formulation. For a transient analysis, it is well known that the pressure formulation results in a non-symmetric matrix. The non-symmetry of the matrix can be removed using the velocity potential formulation or the pressure–displacement potential formulation on the expense of an added damping matrix [7]. One significant disadvantage of the pressure or potential formulation is that they are developed for inviscid fluid only. The displacement formulation can model a viscous fluid, and the coupling condition at the fluid–structure interface can be easily implemented. However, the displacement formulation in the frequency analysis suffers from the

* Corresponding author. Tel.: +1 614 598 1732.
E-mail addresses: lchengz@umich.edu (L. Cheng), r.white@tufts.edu (R.D. White), grosh@umich.edu (K. Grosh).

0045-7825/$ - see front matter Published by Elsevier B.V.
doi:10.1016/j.cma.2008.04.016

presence of the non-zero frequency modes with no physical meaning (i.e. spurious modes [15]), and it locks in the frequency analysis of a solid vibrating in a nearly incompressible fluid [19]. Recently we also found that the displacement formulation locks in the analysis of a nearly incompressible fluid interacting with a flexible boundary [26]. Many researchers have proposed improved formulations to solve this problem (a complete review on this matter can be found in [1]) among which a displacement/pressure based mixed formulation, developed by Bathe [1], has been demonstrated to have no spurious modes with the selection of the proper elements. It is also proven to be effective in the analysis of incompressible or nearly incompressible media. For a three-dimensional problem, the mixed formulation has four degrees of freedom per node in the fluid element, thus a higher computational burden compared with the displacement based formulation. However, for a nearly incompressible fluid, the pressure degrees of freedom can be condensed out in the element level, resulting in the same matrix size as in the displacement based formulation.

The viscous effect can also be included in the fluid model approximately under certain assumptions. Beltman et al. [2] presented a viscothermal acoustic finite element model for acousto-elastic problems with thin layers. The model assumes that the pressure is constant across the layer thickness so that three-dimensional formulation is collapsed to two-dimensional. Beltman's model is only applicable when the viscous boundary layer thickness is comparable to the thickness of the layer. Bossart et al. [5] developed a hybrid numerical and analytical solution for thermo-viscous fluids, in which a modified acoustic boundary condition is derived to account for the fluid viscosity using a boundary layer theory. The pressure formulation is used in this model since the viscous boundary condition is written in terms of pressure and its derivatives only. A similar non-dimensionalized acoustic boundary condition was proposed by Holmes and Cole [13], although it was not implemented in the FEM model. These modified boundary conditions were constructed under the assumption that the viscous boundary layer thickness is small compared to the dimension of the domain. To simulate the frequency response of a coupled fluid–structure system, the boundary layer thickness could vary from big (at low frequencies) to small (at high frequencies) compared to the dimension of the system. Currently the viscous approximations only work at two extreme cases but are not applicable to the problems with intermediate boundary layer thickness although it greatly simplifies the FEM formulation.

In this work, a fully coupled three-dimensional FEM formulation is derived for the analysis of acoustic fluid–structure interaction problems. The fluid is viscous and nearly incompressible. The fluid displacements are very small therefore a linear response can be assumed. The structure has a flat surface and is modeled as a plate with or without residual stress. The displacement pressure based mixed formulation is used to model the fluid field to avoid the locking behavior and to suppress the spurious modes. The coupling condition at the interface is such that the normal velocity and force are continuous but the tangential velocities are negligible. A similar 3D coupled FEM model was developed by Figueroa et al. [8] to simulate the blood flow in the arteries. This study differs from Figueroa's work in the coupling condition at the fluid–structure interface, the structural model and the elements used both in the structure and fluid domains. This model could also find its application in the modeling of the cochlea and cochlear-based transducers. There has been extensive research carried out over the last 60 years attempting to understand the functioning of the cochlea through experiments and mathematical models. A conventional view of the cochlear mechanics can be found in [6] including experimental results and basic modeling techniques. Recent efforts in the cochlear modeling has been focused on developing a physiologically realistic model of the cochlea and numerical methods have become more popular due to their ability to deal with complicated structures. Giverlberg and Bunn [10] developed a full three-dimensional model of the curved cochlea using immersed boundary method [3]. The fluid is modeled as viscous and incompressible using nonlinear Navier–Stokes equation. Their model shows the promise of large scale computational modeling applicable to study the cochlear mechanics, however, the computational cost is very high compared to other 3D models. Parthasarathi et al. [21] proposed an inviscid fluid–structure coupled cochlea model using the pressure formulation. In their model, the fluid domain is meshed in 2D and a finite number of fluid modes is used in the third dimension. The nature of this formulation (i.e. the modal solution in one direction) limits its application in the viscous fluid medium. Two different groups [9,4] used the commercial FEM software package ANSYS to study the passive cochlear mechanics, in which Böhnke and Arnold [4] developed a three-dimensional fluid–structure interaction system with a curved cochlear duct. The fluid is considered inviscid and compressible. Gan et al. [9] built a 3D FEM model of the ear incorporated the ear canal, the middle ear and the straightened cochlea. A more rapid solution can be obtained by a semi-analytic method known as Wentzel–Kramers–Brillouin (WKB) method [16,17,22,24]. Most WKB models in the cochlear mechanics only consider the first wave number in their solutions, which may not capture the complete response of the cochlea [24]. Lim and Steele [17] extended the WKB model to include the fluid viscosity. Although the duct height and width can be slowly-varying in their model, it is still difficult to model a duct with any sudden change in the geometry, which is often seen in the cochlear-based transducers [26].

The organization of this paper is as follows. First we introduce the strong and weak forms for fluid domain, structure domain and the coupling between them. We then specify the interpolations used for fluid and structural elements, and the formulations of the element stiffness matrix. Finally, the results from the 3D FEM model are given in comparison to experimental results and other FEM model results, followed by the conclusions.

2. Finite element framework

Fig. 1 shows a typical geometry of interior structural acoustics problem where the viscous compressible fluid is bounded by solid walls, part of which is occupied by a flat flexible structure. The rigid boundary is denoted as Γ_g and the flexible boundary is denoted as Γ_p. The governing equations for fluid domain and structure domain are discussed next.

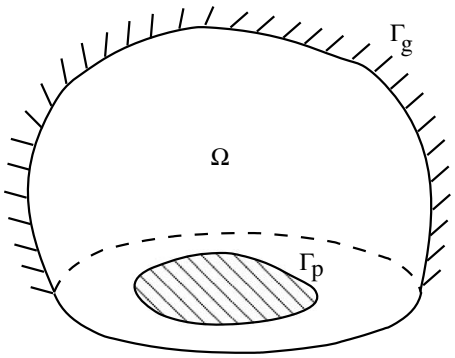

Fig. 1. Geometry of coupled fluid–structure system.

2.1. Fluid domain

Assume that the fluid is viscous and compressible, the motion of the fluid is governed by,

$$\frac{\partial \rho_f}{\partial t} + \rho_f \nabla \cdot \boldsymbol{v} = 0, \tag{1}$$

$$\beta = \frac{1}{\rho_f}\frac{\partial \rho_f}{\partial P}, \tag{2}$$

$$\rho_f\left(\frac{\partial \boldsymbol{v}}{\partial t} + \boldsymbol{v}\cdot\nabla\boldsymbol{v}\right) = -\nabla P + \mu\nabla^2\boldsymbol{v} + \frac{1}{3}\mu\nabla(\nabla\cdot\boldsymbol{v}), \tag{3}$$

where ρ_f is the fluid density and $\boldsymbol{v}$ is the fluid velocity vector with three components. β is the compressibility of the fluid ($\beta = 1/\rho_f c^2$). Eq. (1) is the conservation of the mass equation, Eq. (2) is the definition of the compressibility and Eq. (3) is the conservation of momentum equation (i.e. Navier–Stokes equation). The nonlinear convection term $\boldsymbol{v}\cdot\nabla\boldsymbol{v}$ in the Navier–Stokes equation can be neglected for the acoustic fluid when the fluid velocity is small compared to the dimensions of the model therefore the linearized time harmonic Navier–Stokes equation takes the form,

$$-\rho_f\omega^2\boldsymbol{u} = -\nabla P + \mathrm{j}\omega\mu\nabla^2\boldsymbol{u} + \frac{1}{3}\mathrm{j}\omega\mu\nabla(\nabla\cdot\boldsymbol{u}). \tag{4}$$

Here we restrict our solution to be steady state with an assumed $e^{j\omega t}$ dependence. $\boldsymbol{u}$ is the fluid displacement and we have $\boldsymbol{v} = \partial\boldsymbol{u}/\partial t = \mathrm{j}\omega\boldsymbol{u}$.

Replacing ρ_f by P using the constitutive equation (Eq. (2)), the conservation of the mass equation (Eq. (1)) can be written as,

$$\beta P + \nabla\cdot\boldsymbol{u} = 0. \tag{5}$$

This equation is reduced to

$$\nabla\cdot\boldsymbol{u} = 0, \tag{6}$$

when the fluid is incompressible ($\beta = 0$). Note that we can substitute Eq. (5) into Eq. (4) to cancel out the pressure P so that the linearized Navier–Stokes equation is written only in terms of the fluid displacements. This substitution will lead to the pure displacement based formulation since the only variable in the equation is the fluid displacement. As Bathe [1] pointed out, the pure displacement based formulation tends to lock for a nearly incompressible fluid. To alleviate the locking and improve the accuracy, we can use a mixed formulation in which the pressure and displacement are treated as two independent variables and interpolated independently.

The boundary conditions for the fluid domain can be written as,

$$\begin{aligned} &u_1 = u_2 = u_3 = 0, \quad \text{at } \Gamma_g,\\ &u_1 = u_2 = 0,\ u_3 = w, \quad \text{at } \Gamma_p, \end{aligned} \tag{7}$$

where the subscripts 1 and 2 denote the tangential components of the fluid displacements and 3 denotes normal component. w is the out-of-plane displacement of the structure. At the fluid–structure interface Γ_p, the boundary condition $u_1 = u_2 = 0$ can be relaxed to allow non-zero in-plane displacements if they are non-negligible. Eqs. (4), (5) and (7) complete the strong form of the fluid governing equations and boundary conditions.

Multiplying Eqs. (4) and (5) by the weighting functions ($\bar{\boldsymbol{u}}$ and $\bar{P}$) and integrating over the fluid volume Ω, we obtain the variational form,

$$\begin{aligned} &\int_\Omega \rho_f\omega^2\bar{u}_s u_s\,\mathrm{d}\Omega + \int_\Omega \bar{u}_{s,s}P\,\mathrm{d}\Omega\\ &\quad - \mathrm{j}\omega\mu\sum_{r=1}^{3}\left(\int_\Omega \bar{u}_{s,r}u_{s,r}\,\mathrm{d}\Omega + \frac{1}{3}\int_\Omega \bar{u}_{s,r}u_{r,s}\,\mathrm{d}\Omega\right) - \int_{\Gamma_s}\bar{u}_s P n_s\,\mathrm{d}\Gamma_s\\ &\quad + \mathrm{j}\omega\mu\sum_{r=1}^{3}\left(\int_{\Gamma_r}\bar{u}_s u_{s,r}n_r\,\mathrm{d}\Gamma_r + \frac{1}{3}\int_{\Gamma_r}\bar{u}_s u_{r,s}n_r\,\mathrm{d}\Gamma_r\right) = 0\\ &\quad \text{for } s = 1,\ldots,3 \end{aligned} \tag{8}$$

and

$$\beta\int_\Omega \bar{P}P\,\mathrm{d}\Omega + \sum_{r=1}^{3}\int_\Omega \bar{P}u_{r,r}\,\mathrm{d}\Omega = 0. \tag{9}$$

Here n_r is the unit outward normal. All the surface boundaries are denoted as Γ_s or Γ_r where r and s are indexes (from 1 to 3). Depending on the location of the boundary, it can belong to Γ_g (rigid boundary) or Γ_p (flexible boundary) as shown in Fig. 1. Using the fluid boundary conditions defined in Eq. (7), most of the boundary terms vanish except the normal displacement at the fluid–structure interface Γ_p. The non-zero boundary term is,

$$\int_{\Gamma_p}\bar{u}_3\left(-P + \frac{4}{3}\mathrm{j}\omega\mu u_{3,3}\right)n_3\,\mathrm{d}\Gamma_p \tag{10}$$

with the substitution of $r = 3$, $s = 3$ and $n_r = n_s = -1$ in Eq. (8). This term is related to the surface traction t_3 at $z = 0$. The relation can be established from the definition of the stress tensor in the fluid,

$$\boldsymbol{\sigma} = -P\boldsymbol{I} + \mu\left(\nabla\boldsymbol{v} + \nabla^{\mathrm{T}}\boldsymbol{v} - \frac{2}{3}\nabla\cdot\boldsymbol{v}\boldsymbol{I}\right). \tag{11}$$

Hence at $z = 0$, the stresses are,

$$\sigma_{33} = -P + \frac{4}{3}\mathrm{j}\omega\mu u_{3,3}, \quad \sigma_{31} = \mathrm{j}\omega\mu u_{3,1}, \quad \sigma_{32} = \mathrm{j}\omega\mu u_{3,2}, \tag{12}$$

after applying the boundary condition $u_1 = u_2 = 0$ in Eq. (11).

Therefore Eq. (10) can be written as,

$$\int_{\Gamma_p}\bar{u}_3\left(-P + \frac{4}{3}\mathrm{j}\omega\mu u_{3,3}\right)n_3\,\mathrm{d}\Gamma_p = \int_{\Gamma_p}\bar{u}_3\sum_{r=1}^{3}\sigma_{3r}n_r\,\mathrm{d}\Gamma_p = \int_{\Gamma_p}\bar{u}_3 t_3\,\mathrm{d}\Gamma_p \tag{13}$$

with the traction $t_i = \sum_j \sigma_{ij}n_j$.

2.2. Structure domain

In the structure domain, the most commonly used theories to model a plate are the classical Poisson–Kirchhoff theory and Reissner–Mindlin plate theory. Interpolations of the Kirchhoff plate requires C^1 continuity, while the Mindlin plate requires only C^0 continuity. In order to be compatible with the fluid element which has only C^0 continuity, the Mindlin plate is chosen here for a straightforward implement of the coupling between the fluid and structure domains.

The main assumption for the Mindlin plate is that the normals to the midplane of the plate remain straight during the deformation but they are not necessarily normal to the deformed middle surface. With this assumption, the displacement components can be written as,

$$u_{p1} = -z\theta_x(x,y), \quad u_{p2} = -z\theta_y(x,y), \quad u_{p3} = w(x,y), \tag{14}$$

where θ_x and θ_y are the rotations of the normal to the plate middle surface and w is the plate transverse displacement. Here we assume that the plate is located in the x–y plane. We denote $\boldsymbol{u}_p = (\,\theta_x \quad \theta_y \quad w\,)^{\mathrm{T}}$.

The bending strains and the shear strains can be computed from the displacement components as follows:

$$\begin{pmatrix}\epsilon_{xx}\\ \epsilon_{yy}\\ \gamma_{xy}\end{pmatrix} = -z\boldsymbol{\kappa} = -z\begin{pmatrix}\frac{\partial\theta_x}{\partial x}\\ \frac{\partial\theta_y}{\partial y}\\ \frac{\partial\theta_x}{\partial y} + \frac{\partial\theta_y}{\partial x}\end{pmatrix}, \quad \boldsymbol{\gamma} = \begin{pmatrix}\gamma_{xz}\\ \gamma_{yz}\end{pmatrix} = \begin{pmatrix}\frac{\partial w}{\partial x} - \theta_x\\ \frac{\partial w}{\partial y} - \theta_y\end{pmatrix}. \tag{15}$$

The variation equation of the plate is obtained by substituting the strains into the principle of virtual work, giving,

$$\int_\Gamma \bar{\boldsymbol{\kappa}}^{\mathrm{T}}\boldsymbol{C}_b\boldsymbol{\kappa}\,\mathrm{d}\Gamma + \int_\Gamma \bar{\boldsymbol{\gamma}}^{\mathrm{T}}\boldsymbol{C}_s\boldsymbol{\gamma}\,\mathrm{d}\Gamma + \int_\Gamma \bar{\boldsymbol{u}}_p^{\mathrm{T}}\boldsymbol{M}\boldsymbol{u}_p\,\mathrm{d}\Gamma = \int_\Gamma \bar{w}f_3\,\mathrm{d}\Gamma, \tag{16}$$

where Γ_p has been denoted as Γ for convenience. f_3 is the transverse loading per unit area. $\boldsymbol{C}_b$, $\boldsymbol{C}_s$ and $\boldsymbol{M}$ are defined as,

$$\boldsymbol{C}_b = \frac{t^3}{12}\begin{bmatrix} \frac{E_x}{1-\nu_{xy}\nu_{yx}} & \frac{\nu_{yx}E_x}{1-\nu_{xy}\nu_{yx}} & 0 \\ \frac{\nu_{yx}E_x}{1-\nu_{xy}\nu_{yx}} & \frac{E_y}{1-\nu_{xy}\nu_{yx}} & 0 \\ 0 & 0 & G_{xy} \end{bmatrix}, \quad \boldsymbol{C}_s = ktG_{xy}\begin{bmatrix} 1 & 0 \\ 0 & 1 \end{bmatrix},$$
$$\boldsymbol{M} = -\rho_p\omega^2\begin{bmatrix} \frac{t^3}{12} & 0 & 0 \\ 0 & \frac{t^3}{12} & 0 \\ 0 & 0 & t \end{bmatrix}, \tag{17}$$

for an orthotropic plate. E_x, E_y and G_{xy} are the Young's moduli and shear modulus. ν_{xy} and ν_{yx} are the Poisson's ratios. ρ_p is the plate density and t is the plate thickness. k is a constant to account for the actual non-uniformity of the shearing stress and k is usually taken to be 5/6 [1].

The boundary conditions for a simply-supported plate are: $w = 0$, θ_x and θ_y are free [14] at the edges.

2.3. Coupling between two domains

The coupling between the fluid and structure domains is realized through the forcing terms. Since we have already neglected the in-plane displacements at the fluid–structure interface, the coupling occurs only in the normal direction. We know that the surface traction acting on the fluid due to the interaction with the structure is equal and opposite to the pressure loading on the structure by the fluid, i.e. $t_3 = -f_3$, and the continuity in the normal velocity at the interface gives $u_3 = w$. Using these two equations, we have

$$\int_\Gamma \bar{u}_3 t_3 \,\mathrm{d}\Gamma = -\int_\Gamma \bar{w} f_3 \,\mathrm{d}\Gamma. \tag{18}$$

Hence the final form of the variational equations for the coupled system, if written in terms of the displacement components and pressure, is,

$$\begin{aligned}
&\int_\Omega \rho_f\omega^2\bar{u}_1u_1\,\mathrm{d}\Omega + \int_\Omega \bar{u}_{1,1}P\,\mathrm{d}\Omega - \mathrm{j}\omega\mu\int_\Omega(\bar{u}_{1,1}u_{1,1}+\bar{u}_{1,2}u_{1,2}+\bar{u}_{1,3}u_{1,3})\,\mathrm{d}\Omega \\
&\quad -\frac{1}{3}\mathrm{j}\omega\mu\int_\Omega(\bar{u}_{1,1}u_{1,1}+\bar{u}_{1,2}u_{2,1}+\bar{u}_{1,3}u_{3,1})\,\mathrm{d}\Omega = 0, \\
&\int_\Omega \rho_f\omega^2\bar{u}_2u_2\,\mathrm{d}\Omega + \int_\Omega \bar{u}_{2,2}P\,\mathrm{d}\Omega - \mathrm{j}\omega\mu\int_\Omega(\bar{u}_{2,1}u_{2,1}+\bar{u}_{2,2}u_{2,2}+\bar{u}_{2,3}u_{2,3})\,\mathrm{d}\Omega \\
&\quad -\frac{1}{3}\mathrm{j}\omega\mu\int_\Omega(\bar{u}_{2,1}u_{1,2}+\bar{u}_{2,2}u_{2,2}+\bar{u}_{2,3}u_{3,2})\,\mathrm{d}\Omega = 0, \\
&\int_\Omega \rho_f\omega^2\bar{u}_3u_3\,\mathrm{d}\Omega + \int_\Omega \bar{u}_{3,3}P\,\mathrm{d}\Omega - \mathrm{j}\omega\mu\int_\Omega(\bar{u}_{3,1}u_{3,1}+\bar{u}_{3,2}u_{3,2}+\bar{u}_{3,3}u_{3,3})\,\mathrm{d}\Omega \\
&\quad -\frac{1}{3}\mathrm{j}\omega\mu\int_\Omega(\bar{u}_{3,1}u_{1,3}+\bar{u}_{3,2}u_{2,3}+\bar{u}_{3,3}u_{3,3})\,\mathrm{d}\Omega - \int_\Gamma \bar{\boldsymbol{\kappa}}^{\mathrm{T}}\boldsymbol{C}_b\boldsymbol{\kappa}\,\mathrm{d}\Gamma \\
&\quad -\int_\Gamma \bar{\boldsymbol{\gamma}}^{\mathrm{T}}\boldsymbol{C}_s\boldsymbol{\gamma}\,\mathrm{d}\Gamma - \int_\Gamma \bar{\boldsymbol{u}}_p^{\mathrm{T}}\boldsymbol{M}\boldsymbol{u}_p\,\mathrm{d}\Gamma = 0,
\end{aligned} \tag{19}$$

along with Eq. (9).

If the residual stress in the structure is non-negligible compared to the bending effect, we should also include the tension effect in the structure governing equation. Assume that the tensions in the structure are T_x and T_y (they are not necessarily the same), the third equation in Eq. (19) is changed to,

$$\begin{aligned}
&\int_\Omega \rho_f\omega^2\bar{u}_3u_3\,\mathrm{d}\Omega + \int_\Omega \bar{u}_{3,3}P\,\mathrm{d}\Omega - \mathrm{j}\omega\mu\int_\Omega(\bar{u}_{3,1}u_{3,1}+\bar{u}_{3,2}u_{3,2} \\
&\quad +\bar{u}_{3,3}u_{3,3})\,\mathrm{d}\Omega - \frac{1}{3}\mathrm{j}\omega\mu\int_\Omega(\bar{u}_{3,1}u_{1,3}+\bar{u}_{3,2}u_{2,3}+\bar{u}_{3,3}u_{3,3})\,\mathrm{d}\Omega \\
&\quad +\int_\Gamma(T_x\bar{u}_{3,1}u_{3,1}+T_y\bar{u}_{3,2}u_{3,2})\,\mathrm{d}\Gamma - \int_\Gamma \bar{\boldsymbol{\kappa}}^{\mathrm{T}}\boldsymbol{C}_b\boldsymbol{\kappa}\,\mathrm{d}\Gamma - \int_\Gamma \bar{\boldsymbol{\gamma}}^{\mathrm{T}}\boldsymbol{C}_s\boldsymbol{\gamma}\,\mathrm{d}\Gamma \\
&\quad -\int_\Gamma \bar{\boldsymbol{u}}_p^{\mathrm{T}}\boldsymbol{M}\boldsymbol{u}_p\,\mathrm{d}\Gamma = 0.
\end{aligned} \tag{20}$$

We can see from the above equation that the structure degrees of freedom are only coupled to the fluid displacement in the z direction, and the coupling only affects the fluid elements at the fluid–structure interface. There are two approaches to deal with the coupling effects in the FEM discretization. The first one is to construct the fluid element at the fluid–structure interface separately so that its stiffness matrix can include the contribution from the structure besides those from the fluid. The second one is to construct a coupling element at the interface to include only the coupling effect from the structure so that the fluid element at the interface is the same as those in the domain. The second approach is used in this work and the main advantage for constructing a coupling element is that the fluid element at the interface does not change with the mechanics of the structure. If the structure governing equation or the coupling mechanics is changed, we only need to generate a new coupling element. Next we will cover the basics for constructing the fluid element, the structure element and the coupling element.

3. The choices of elements

Selecting the proper elements is essential to achieve accurate and converged results in the FEM formulation. In the fluid domain, we choose to use a 27/4 u/p mixed element [1] in which the displacement interpolation is tri-quadratic while the pressure is linearly interpolated. In the structure domain, the 9-noded Hinton–Huang's element is used in order to be compatible with fluid element. The description of each element is detailed next.

3.1. Fluid elements

In the displacement/pressure based mixed formulation, we interpolate not only the displacement but also the pressure. Since the pressure has the same order as the volume strain, its interpolation should be of lower order than the displacement. The simplest possible fluid element is a 8-noded brick element in which the displacement is linearly interpolated and the pressure is constant inside the element. This element is denoted as 8/1 u/p element and has been shown to be reasonably good, according to Bathe [1]. However, it does not satisfy the inf–sup condition, a criterion to determine whether an element is stable and convergent [1], and also exhibits a spurious mode for a specific mesh with certain boundary conditions. The 8/1 u/p element is actually equivalent to a 8-noded pure displacement based element with reduced integration on the compressibility term [14], which exhibits locking behavior at low frequencies for the example problem shown in this paper (see Section 5 for more details).

Considering a higher-order displacement interpolation such as tri-quadratic interpolation (corresponding to a 27-noded element for the displacement), the pressure interpolation has several choices including a constant, linear or trilinear interpolations. The study [1] shows that the element with tri-quadratic displacement and linear pressure gives the best overall performance among these choices and it is named as 27/4 u/p mixed element since the pressure interpolation has four unknowns: $P = p_0 + p_1x + p_2y + p_3z$.

To obtain the governing finite element equations for the fluid, here we will show the formulation of the stiffness matrix for one single element. Assembling the global matrix from the element matrix can be performed in a standard manner. For a 27/4 u/p element, we assume that the displacement and pressure interpolations are,

$$\boldsymbol{u} = \boldsymbol{N}_u\hat{u}, \quad P = \boldsymbol{N}_p\widehat{P} \tag{21}$$

with

$$\boldsymbol{N_u} = \begin{bmatrix} N_u^1 & 0 & 0 & N_u^2 & 0 & 0 & \cdots & N_u^{27} & 0 & 0 \\ 0 & N_u^1 & 0 & 0 & N_u^2 & 0 & \cdots & 0 & N_u^{27} & 0 \\ 0 & 0 & N_u^1 & 0 & 0 & N_u^2 & \cdots & 0 & 0 & N_u^{27} \end{bmatrix},$$
$$\hat{\boldsymbol{u}} = [\, u_1^1 \quad u_2^1 \quad u_3^1 \quad u_1^2 \quad u_2^2 \quad u_3^2 \quad \cdots \quad u_1^{27} \quad u_2^{27} \quad u_3^{27} \,]^{\mathrm{T}}, \tag{22}$$
$$\widehat{\boldsymbol{P}} = [\, P_0 \quad P_1 \quad P_2 \quad P_3 \,]^{\mathrm{T}},$$

where N_u^1 to N_u^{27} are the shaping functions for a 27-noded trilinear element and $\hat{\boldsymbol{u}}$ is the nodal displacement vector. The superscript and subscript in u_1^2 denote the nodal number and the displacement component, respectively (e.g., u_1^2 is the fluid displacement in the x direction at node 2). $\widehat{\boldsymbol{P}}$ is the unknown pressure vector. Note that $\widehat{\boldsymbol{P}}$ does not correspond to any nodal pressure. Using this interpolation, the pressure is continuous inside the element but discontinuous across the element. Substituting the interpolations into the fluid variational equation (Eq. (19)), we can obtain the element stiffness matrix,

$$\boldsymbol{K}^{\mathrm{e}} \begin{pmatrix} \hat{\boldsymbol{u}} \\ \widehat{\boldsymbol{P}} \end{pmatrix} = \begin{bmatrix} \boldsymbol{K}_{uu}^{\mathrm{e}} & \boldsymbol{K}_{up}^{\mathrm{e}} \\ \boldsymbol{K}_{pu}^{\mathrm{e}} & \boldsymbol{K}_{pp}^{\mathrm{e}} \end{bmatrix} \begin{pmatrix} \hat{\boldsymbol{u}} \\ \widehat{\boldsymbol{P}} \end{pmatrix} = \begin{pmatrix} \boldsymbol{R} \\ \boldsymbol{0} \end{pmatrix}, \tag{23}$$

where

$$\boldsymbol{K}_{up}^{\mathrm{e}} = (\boldsymbol{K}_{pu}^{\mathrm{e}})^{\mathrm{T}} = \int_{\Omega} \boldsymbol{B}_v^{\mathrm{T}} \boldsymbol{N}_p \, \mathrm{d}\Omega,$$
$$\boldsymbol{K}_{pp}^{\mathrm{e}} = \beta \int_{\Omega} \boldsymbol{N}_p^{\mathrm{T}} \boldsymbol{N}_p \, \mathrm{d}\Omega \tag{24}$$

and

$$\boldsymbol{B}_v = \left[\frac{\partial N_u^1}{\partial x} \quad \frac{\partial N_u^1}{\partial y} \quad \frac{\partial N_u^1}{\partial z} \quad \frac{\partial N_u^2}{\partial x} \cdots \quad \frac{\partial N_u^{27}}{\partial z} \right]. \tag{25}$$

The expression for $\boldsymbol{K}_{uu}^{\mathrm{e}}$ can be obtained from the fluid governing equation directly and is omitted here. Since the pressure degrees of the freedom $\widehat{\boldsymbol{P}}$ are only pertain to one element, we can solve the pressure unknowns using the second equation in Eq. (23),

$$\widehat{\boldsymbol{P}} = -(\boldsymbol{K}_{pp}^{\mathrm{e}})^{-1} \boldsymbol{K}_{pu}^{\mathrm{e}} \hat{\boldsymbol{u}}, \tag{26}$$

substituting this equation into the first equation in Eq. (23), we obtain the new element stiffness matrix which is only related to the nodal displacement:

$$\overline{\boldsymbol{K}}^{\mathrm{e}} = \boldsymbol{K}_{uu}^{\mathrm{e}} - \boldsymbol{K}_{up}^{\mathrm{e}} (\boldsymbol{K}_{pp}^{\mathrm{e}})^{-1} (\boldsymbol{K}_{pu}^{\mathrm{e}}), \tag{27}$$

so that the pressure degrees of freedom are condensed out on the element level. Note this stiffness matrix is different from the one in the pure displacement based formulation although the unknowns in the final equation are both nodal displacements. The pressure unknowns are canceled out in the weak form and the pressure is interpolated independently. The forcing term in the fluid variational equation will be considered in the next section in the coupling elements.

4. Structural/coupling element

Similar to the fluid element, the pure displacement based plate elements tend to be overly constrained and exhibit a strong artificial stiffening in the thin plate limit. To alleviate the effect of shear locking in the plate element, different interpolations are used for the bending and shear strains. In order to be compatible with three-dimensional 27-noded fluid element, the structural element should have 9 nodes with bilinear interpolation for the transverse displacement. There are two groups of 9-noded structural elements shown to be efficient and reliable with a mixed interpolation for bending and shear strains: MITC9 element (MITC stands for mixed interpolation of tensorial components) [1] and Hinton–Huang's 9-noded plate element [12]. Unfortunately the MITC9 element uses a serendipity type interpolation for transverse displacement (8 nodes for the displacement and 9 nodes for section rotations) which makes it incompatible with the fluid element. In this paper, we use Hinton–Huang's Lagrangian element for the coupled analysis.

Following the general methodology proposed by Onate et al. [20] for deriving Hinton and Huang's plate element, the shear strains are interpolated independently with the following form:

$$\gamma_\xi = a_1 + a_2\xi + a_3\eta + a_4\xi\eta + a_5\eta^2 + a_6\xi\eta^2,$$
$$\gamma_\eta = b_1 + b_2\xi + b_3\eta + b_4\xi\eta + b_5\xi^2 + b_6\eta\xi^2 \tag{28}$$

and they were written in terms of ξ and η in the natural coordinates: $\xi \in [-1, 1]$ and $\eta \in [-1, 1]$ (see Fig. 2). The Cartesian shear strains are related to natural shear strains via Jacobian matrix $\boldsymbol{J}$. The unknowns a_1 to a_6 and b_1 to b_6 are solved by strongly enforcing

$$\gamma_\xi = \frac{\partial w}{\partial \xi} - \theta_\xi, \quad \gamma_\eta = \frac{\partial w}{\partial \eta} - \theta_\eta, \quad \text{see Eq.(15)} \tag{29}$$

at 12 sampling points shown in Fig. 2 (six sampling points for γ_ξ and six for γ_η). This will generate 12 equations to solve for the coefficients a_1 to a_6 and b_1 to b_6 so that the element shear strains can be expressed in terms of $(w, \theta_\xi, \theta_\eta)$ at those 12 points, which are again related to the nodal displacements and no more unknowns are introduced for shear strains in the element stiffness matrix.

Therefore the final element stiffness matrix for the 9-noded Mindlin plate element is,

$$\boldsymbol{K}^{\mathrm{e}} = \boldsymbol{K}_{\mathrm{b}}^{\mathrm{e}} + \boldsymbol{K}_{\mathrm{s}}^{\mathrm{e}} + \boldsymbol{K}_{m}^{\mathrm{e}} \tag{30}$$

and

$$\boldsymbol{K}_{\mathrm{b}}^{\mathrm{e}} = \int_{\Gamma} \boldsymbol{B}_{\mathrm{b}}^{\mathrm{T}} \boldsymbol{C}_{\mathrm{b}} \boldsymbol{B}_{\mathrm{b}} \, \mathrm{d}\Gamma, \quad \boldsymbol{K}_{\mathrm{s}}^{\mathrm{e}} = \int_{\Gamma} \overline{\boldsymbol{B}}_s^{T} \boldsymbol{C}_s \overline{\boldsymbol{B}}_s \, \boldsymbol{d}\Gamma, \quad \boldsymbol{K}_{\boldsymbol{m}}^{e} = \int_{\Gamma} \boldsymbol{N}^{T} \boldsymbol{M} \boldsymbol{N} \, \boldsymbol{d}\Gamma, \tag{31}$$

where $\boldsymbol{B}_{\mathrm{b}}$ and $\overline{\boldsymbol{B}}_s$ are plate bending and shear stiffness matrices, respectively. Note that $\boldsymbol{B}_{\mathrm{b}}$ can be directly computed from Eq. (16) but $\overline{\boldsymbol{B}}_s$ is calculated from the different interpolation introduced above.

For a thin plate, we can assume that the in-plane displacements are small and the fluid and the structure are coupled at the plate midplane. The continuity of the displacements at the interface gives

$$u_{p1} = u_1 = 0, \quad u_{p2} = u_2 = 0, \quad w = u_3. \tag{32}$$

Note that at the structure midplane, the in-plane displacements are zero but the rotations θ_x and θ_y are not necessarily zero (see Eq. (14)).

Normally for fluid–structure interaction problems, the coupling between fluid and structure domains can be easily implemented with the displacement formulation and the stiffness contribution

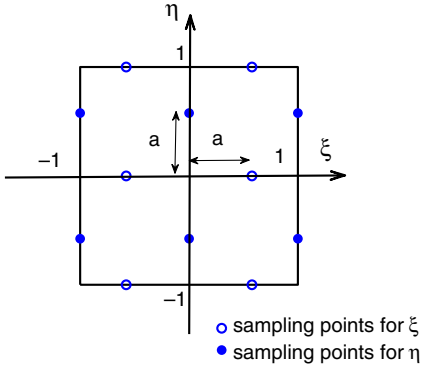

Fig. 2. The positions of 12 sampling points in a 9-noded Mindlin plate element ($a = 1/\sqrt{3}$).

from the structure can be directly added to the fluid stiffness matrix at the corresponding nodes at the interface. However, this is not the case in our problem since there is no direct coupling between (u_1, u_2) and (θ_x, θ_y) at the interface. We need to construct a new element which can couple the structural degrees of freedom (w, θ_x, θ_y) to the fluid degrees of freedom (u_1, u_2, u_3) at the interface and also account for the plate stiffness contribution in the variational equation (Eq. (19)). The coupling element has 18 nodes with 9 structural nodes on the bottom plane (numbered 1–9) and 9 fluid nodes on the top (numbered 10–18), as shown in Fig. 3. Since all the nodes are located at the plate midplane and the element has zero thickness, node 1 and node 10 have exactly the same coordinates, so do node 2 and node 11, and etc. The degrees of freedom for the bottom nodes are (θ_x, θ_y) and (u_1, u_2, u_3) for the top nodes. Note that the bottom nodes only have two degrees of freedom instead of three in the plate element, because at the interface we have $u_3 = w$ so only one of them needs to be included in the element. The nodal degrees of freedom for one single coupling element is,

$$\hat{\boldsymbol{u}}_c = \begin{bmatrix} \theta_x^1 & \theta_y^1 & \cdots & \theta_x^9 & \theta_y^9 & u_1^{10} & u_2^{10} & u_3^{10} & \cdots & u_1^{18} & u_2^{18} & u_3^{18} \end{bmatrix}. \tag{33}$$

With the use of the new element, at the interface we have fluid element which is the same as the ones in the domain and also a zero-thickness coupling element with top 9 nodes the same as fluid nodes and bottom 9 nodes for plate rotations. The third equation in Eq. (19) shows that the deformation of the structure is coupled to the fluid domain as a boundary condition and the coupling only occurs between θ_x, θ_y and u_3 (i.e. w). The coupling element stiffness matrix $\boldsymbol{K}_c^e$ is just an expansion of the stiffness matrix for structural elements with extra zeros at the rows and columns related to u_1 and u_2,

$$\boldsymbol{K}_c^e = \begin{bmatrix} \boldsymbol{K}_{\theta\theta}^e & \boldsymbol{K}_{\theta w}^e \\ \boldsymbol{K}_{w\theta}^e & \boldsymbol{K}_{ww}^e \end{bmatrix} \tag{34}$$

with

$$\boldsymbol{K}_{\theta\theta}^e = \begin{bmatrix} k_{11} & k_{12} & k_{14} & k_{15} & \cdots & k_{1,26} \\ & k_{22} & k_{24} & k_{25} & \cdots & k_{2,26} \\ & & k_{44} & k_{45} & \cdots & k_{4,26} \\ & \text{symm.} & & k_{55} & \cdots & k_{5,26}, \\ & & & & \ddots & \vdots \\ & & & & & k_{26,26} \end{bmatrix}_{18\times 18}, \tag{35}$$

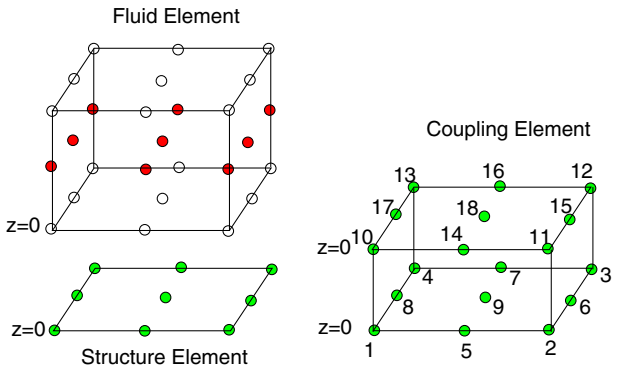

Fig. 3. Fluid element, structure element and coupling element at the fluid–structure interface.

$$\boldsymbol{K}_{ww}^e = \begin{bmatrix} 0 & 0 & 0 & 0 & 0 & 0 & \cdots & 0 \\ & 0 & 0 & 0 & 0 & 0 & \cdots & 0 \\ & & k_{33} & 0 & 0 & k_{36} & \cdots & k_{3,27} \\ & & & 0 & 0 & 0 & \cdots & 0 \\ & & \text{symm.} & 0 & 0 & \cdots & 0 & \\ & & & & & k_{66} & \cdots & k_{6,27} \\ & & & & & & \ddots & \vdots \\ & & & & & & & k_{27,27} \end{bmatrix}_{27\times 27}, \tag{36}$$

$$\boldsymbol{K}_{\theta w}^e = (\boldsymbol{K}_{w\theta}^e)^{\mathrm{T}} = \begin{bmatrix} 0 & 0 & k_{13} & 0 & 0 & k_{16} & \cdots & k_{1,27} \\ 0 & 0 & k_{23} & 0 & 0 & k_{26} & \cdots & k_{2,27} \\ 0 & 0 & k_{43} & 0 & 0 & k_{46} & \cdots & k_{4,27} \\ 0 & 0 & k_{53} & 0 & 0 & k_{56} & \cdots & k_{5,27} \\ \vdots & \vdots & \vdots & \vdots & \vdots & \vdots & \vdots & \vdots \\ 0 & 0 & k_{26,3} & 0 & 0 & k_{26,6} & \cdots & k_{26,27} \end{bmatrix}_{18\times 27}, \tag{37}$$

where k_{ij} is the (i,j)th component of the plate element stiffness matrix $\boldsymbol{K}^e$ (see Eq. (30)). We can see that in the coupling element stiffness matrix, θ_x and θ_y are not coupled to u_1 and u_2, because the coupling element is constructed on the plate midplane and the in-plane displacements for the fluid and structure are all zero at the interface. As an alternative, Figueroa et al. [8] proposed a different coupling element in which they neglect the variations of the structure in-plane displacements across the thickness so that the coupling conditions at the interface can be written as

$$\begin{aligned} &u_{p1} = u_1, \quad u_{p2} = u_2, \quad w = u_3, \\ &f_1 = -t_1, \quad f_2 = -t_2, \quad f_3 = -t_3 \end{aligned} \tag{38}$$

and this slightly modifies the variational statement in Eq. (19).

5. Results and discussion

In this section, some specific results for three-dimensional FEM computations of fluid–structure interaction are given using the formulation described in this paper. These results are compared to experimental results for steady state vibration of microscale fluid–structure systems as well as to computational results achieved using two lower-dimensional finite element schemes.

Both of the lower-dimensional finite element schemes include full fluid–structure coupling. The first of these was described by Parthasarathi et al. [21]. It is an inviscid, harmonic, pressure-based model that uses a full fluid mesh for pressure in two dimensions, but a finite number of inviscid fluid modes in the third dimension. A single structural cross-mode shape is used, and the structural motion is fully meshed in one dimension only. We refer to this as 2.5D FEM. The second two-dimensional scheme is a thin-film viscoacoustic model taken from the work of Beltman et al. [2]. This approach uses a two-dimensional mesh for both the fluid and structural vibration, but assumes that the fluid film is very thin, resulting in a single pressure dependent variable for the fluid. Fluid viscosity is included in Beltman's model.

The 3D FEM model described in this paper can be used in many acoustic fluid–structure interaction problems in which the linearized Navier–Stokes equation is applicable. For an example of the capabilities, we choose to compare our model results to the fluid–structure traveling waves in hydromechanical cochlear models. The authors have designed, built and tested a number of such models. Fig. 4 shows the typical geometry of the cochlear-based transducers. The fluid-filled cochlear duct is idealized as a single rectangular fluid filled duct. A flexible structure, which mimics the flexible basilar membrane (BM) in the cochlea, occupies part of the bottom wall. The width of this membrane structure varies along the length of the duct. The acoustic input to the system is applied through another rectangular flexible membrane on the

bottom wall, which we refer to as the "input membrane". All other walls of the duct are considered to be rigid. We define the coordinate axes as follows: the x-axis extends longitudinally along the duct length. The y-axis is oriented across the width of the membrane, thus the membrane lies in the x–y plane. The z-axis is normal to the membrane, that is, it defines the height of the duct. The geometry is symmetric about the x–z plane, thus only half of the geometry is modeled with symmetry boundary conditions specified on $y = 0$. The geometric and material properties used in the example problems are given in Fig. 5 and Table 1.

The fluid chamber is micromachined from glass and anodically bonded to a thick silicon die which supports the membrane structures. The basilar membrane is a composite structure composed of a 300 nm thick stoichiometric silicon nitride thin film etched into parallel beams overlayed with a 1.4 μm thick polyimide layer (PI2737 from HD Microsystems, Parlin, NJ). This results in a tensioned orthotropic structure with a tension of approximately 240 N/m in the y direction and 30 N/m in the x direction, as determined by wafer curvature measurements on the unpatterned films. The basilar membrane structure is 30 mm long, and tapers exponentially in width from 0.14 mm to 1.82 mm, as shown in Fig. 5. The input membrane is a rectangle, 1.1 mm × 2.1 mm. The fluid duct is filled with silicone oil with a viscosity of 5 cSt and a density of 911 kg/m^3. Fluid–structure traveling waves and structural vibration are excited by exposing the input membrane to air borne sound delivered by a tweeter. Measurement of the vibration response of the basilar membrane is carried out at steady state using a microscale scanning laser vibrometer and a lock-in amplifier.

Fig. 6a shows the measured magnitude of structure displacement normalized to the driving pressure from the input membrane at 4.2 kHz, 12 kHz and 35 kHz. These results have been published previously in [25]. The corresponding model results calculated from the mixed 3D FEM formulation are shown in Fig. 6b. For all three frequencies, the fluid domain is meshed using 603 nodes in the length direction, 15 nodes in the width direction and 13 nodes in the height direction. The basilar membrane is meshed using 501 × 7 uniform grid and the input membrane is meshed using 43 × 11 uniform grid. The model correctly captures the location of the maximum response and the wave decay after the peak as well as making a good prediction of the magnitude of the response. Any discrepancies between the modeled and measured response magnitude can be attributed to uncertainties in the driving pressure, which cannot be measured exactly at the input membrane. There is also very good agreement between experimental and FEM model results showing the phase of the structural vibration along the membrane centerline (along the x-axis) at three frequencies, as shown in Fig. 7. Note that for this system, the compliance of the BM is about two to three orders of magnitude lower than that of the real cochlea [25], so that the bandwidth of the model shifts towards slightly ultrasonic regime (4–35 kHz).

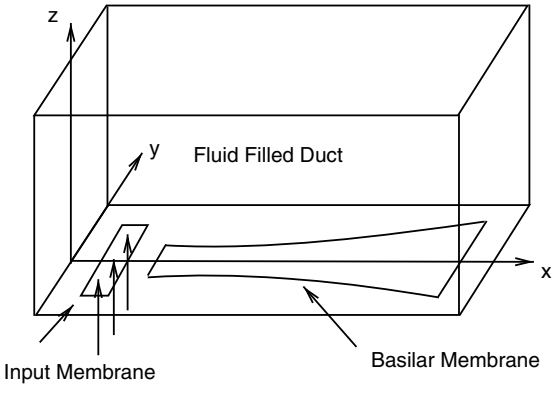

Fig. 4. Geometry of coupled fluid–structure system.

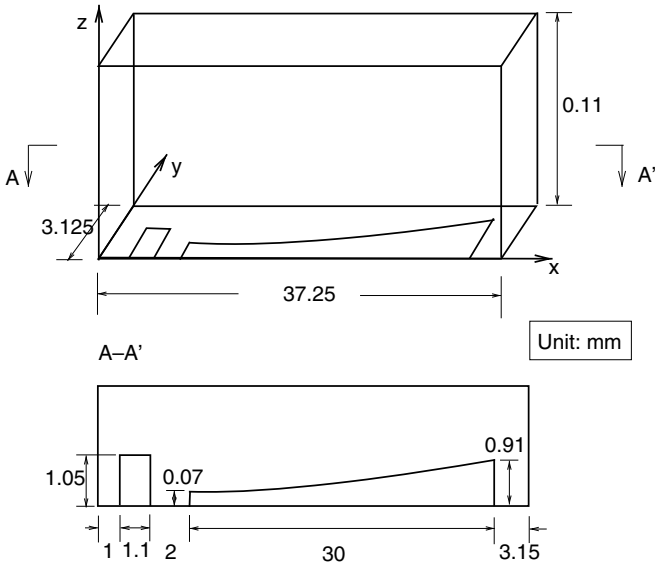

Fig. 5. The dimension of the duct and the structure. The thickness of the structure is 0.32 μm.

Table 1
Material properties for the example problem

Symbols	Value	Unit	Physical meaning
ρ_f	911	kg/m^3	Fluid density
c	1000	m/s	Fluid wave speed
μ	5	cSt	Fluid viscosity
ρ_p	3.6×10^{-3}	kg/m^2	Plate area density
E_x	20	GPa	Young's modulus in x
E_y	160	GPa	Young's modulus in y
ν	0.3		Poisson's ratio
T_x	30	N/m	Tension in x
T_y	240	N/m	Tension in y
η	0.01		Structural damping

For comparison, Fig. 8 shows the computational results from a pure displacement based 3D finite element formulation. This inferior model uses an 8-noded brick element in the fluid domain with trilinear interpolation for the displacement. The FEM mesh uses the same number of the nodes as in the above example (which means that the number of the elements is doubled in each direction). For the terms involving the fluid compressibility, a one point quadrature rule is applied, while the other terms use 2 × 2 × 2 Gaussian quadrature. This selective reduced integration scheme is used in an attempt to alleviate the element locking due to the nearly incompressible fluid. However, at the low frequencies such as 4.2 kHz, the pure displacement based formulation still locks if compared with the results from the mixed FEM model in Fig. 6b. At 12 kHz, it predicts a smaller displacement magnitude than that of the mixed model and the location of the peak is more towards the base of the duct. As mentioned earlier, this 8-noded displacement based formulation is equivalent to an 8/1 displacement/pressure mixed formulation and does not satisfy inf–sup condition, meaning the element is not stable. Although it is very simple to implement and gives a good prediction of the response at some frequencies, such as 35 kHz, the behavior of this formulation is not predictable as we do not know when it will lock and produce meaningless results. In contrast, the 27/4 mixed 3D formulation

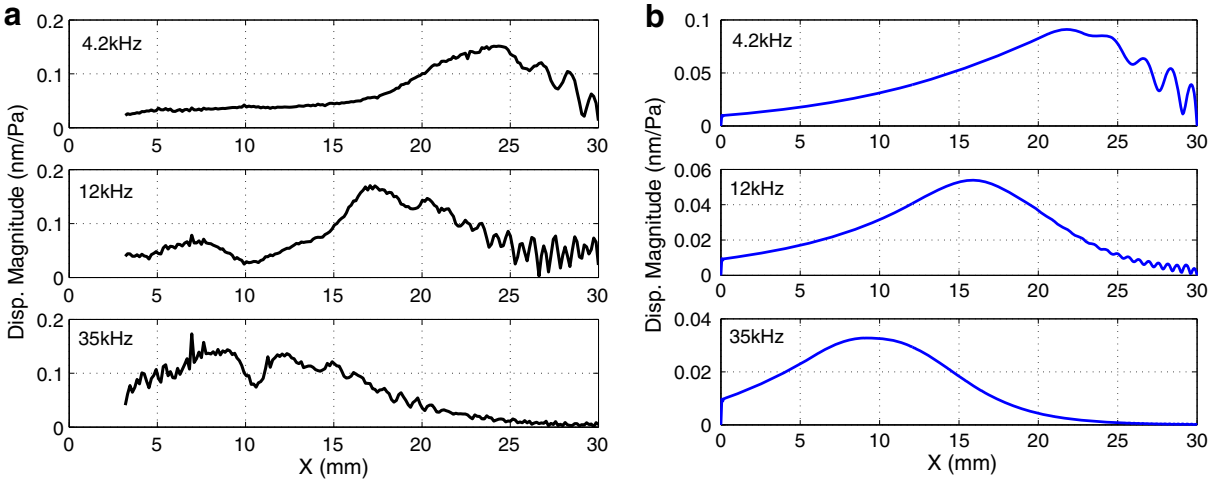

Fig. 6. The magnitude of structure displacement at three different frequencies: (a) the experimental results [25]; (b) the model results from the displacement/pressure mixed formulation which uses the 27/4 u/p element for the fluid and the 9-noded Hinton–Huang's element for the structure. Note that due to optical constraints the entire basilar membrane is not imaged in the experiments; the data starts at 4 mm from the narrow end of the device.

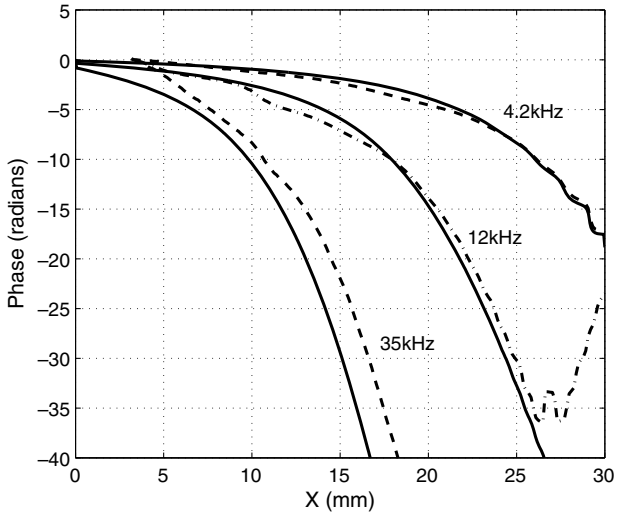

Fig. 7. Comparison of the phase of structure displacement at three different frequencies between the experimental results (dashed line) and the model results (solid line). The experimental data are reference to the phase at 4 mm from the narrow end of the device.

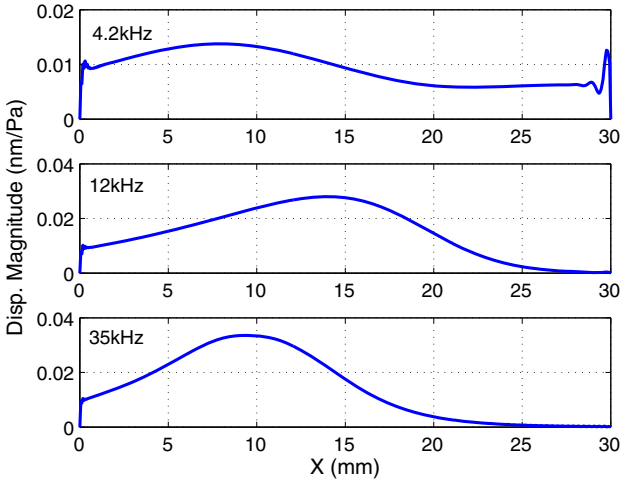

Fig. 8. The magnitude of structure displacement calculated from a pure displacement based formulation with 8-noded fluid elements and selectively reduced integration scheme.

described in this paper gives excellent results at all frequencies although the computational cost is higher.

The convergence of the 3D mixed FEM model is discussed next. As an example, Fig. 9 shows the structure displacement at 4.2 kHz using four different meshes: the original mesh we used in the Fig. 6, doubling the elements in the length, width and height direction respectively. Due to the limitation of our current computational resources (maximum memory 64 GB), it is not feasible to have even more refined mesh without exceeding the memory requirement. However, the converged results in Fig. 9 suggests that the mesh resolution in the above example is sufficient.

Fig. 10 shows the comparison of the structure displacement computed from the 2.5D FEM [21] model and the 3D FEM model at 12 kHz (Fig. 10a) and 35 kHz (Fig. 10b), respectively. For the 3D FEM model, the fluid domain is again meshed using 603 nodes in the x direction, 15 nodes in the y direction and 13 nodes in the z direction, the basilar membrane is meshed using 501×7 uniform grid and the input membrane is meshed using 43×11 unform

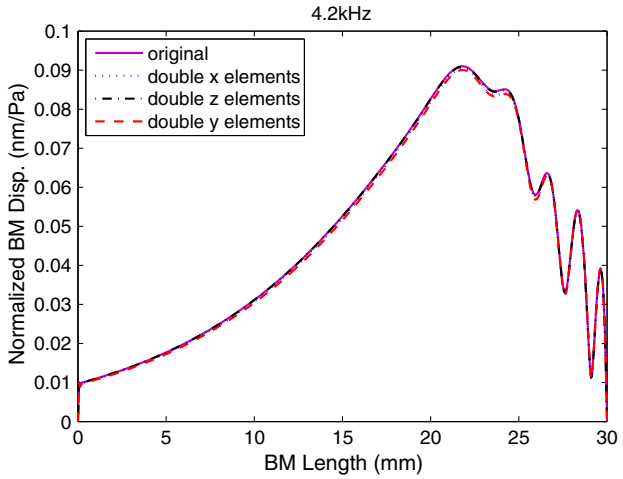

Fig. 9. The magnitude of structure displacement at 4.2 kHz calculated by mixed 3D FEM formulation using four different meshes.

grid. For the 2.5D FEM model, the fluid domain is meshed using 603 x nodes and 42 z nodes. Eight cross-modes is used in the y direction. The structure has 501 nodes in the x direction with only one cross-mode. The 2.5D FEM formulation uses the modal solution in the y direction with a pressure formulation and therefore it only needs a two-dimensional mesh in the x–z plane, big savings in the computational cost but it can only model inviscid fluid, a major drawback. For a fair comparison we must therefore set $\mu = 0$ in the 3D FEM model and instead add structural damping in an *ad hoc* fashion ($\eta = 0.05$) to reduce the reflections from the boundary. The results in Fig. 10b show that there are strong standing waves formed at the end of the structure at 12 kHz, indicating that the structure damping is still not high enough to suppress all the reflections. The mesh resolution is about 11 nodes per wavelength at the place where the wavelength is shortest. The results from the 2.5D FEM model are in a fairly good agreement with 3D FEM results at both frequencies, although there are slight differences in the peak and magnitude of the structure displacements. The discrepancy could be a result of the presence of the higher cross-modes in the input membrane, as shown in Fig. 11. The width of the input membrane is two times larger than its length, so we expect to see higher modes appearing first in the width direction. At 35 kHz, Fig. 11b clearly shows that the displacement in the input membrane has broken into higher cross-modes, although the slender-shaped BM is still dominated by the first cross-mode (Fig. 12). It is, of course, possible for the BM to have higher cross-modes at higher frequencies, and those modes will first appear at the wider end of the structure.

Fig. 13 shows the structure displacement calculated from Beltman's thin film viscothermal acoustic model and the 3D FEM model at 12 kHz. For the 3D FEM model, the fluid domain is meshed using 603 x nodes, 15 y nodes and 21 z nodes, and the basilar membrane and the input membrane are meshed using 501×7 and 43×11 uniform grid, respectively. In the Beltman's thin film model, only two-dimensional mesh in the x–y plane is needed, and in this example, the mesh is the same as that of the 3D FEM model in the x–y plane. As mentioned before, Beltman's model assumes that the pressure is constant across the height of the duct, and thus it may only be applied to structural acoustic systems with thin gaps. The boundary layer thickness, $\delta = \sqrt{\mu/\rho_f \omega}$, is required to be of the same magnitude or larger than the height of the duct. In order to test the effects of violating this requirement, a model case with 474 μm high duct is compared with the results for a 110 μm high duct. The results appear in Fig. 13. Fig. 13a shows an excellent agreement between Beltman's model and 3D FEM model with the smaller duct height, while in Fig. 12b, the Beltman's model seems to provide less damping to the system so that the displacement magnitude is higher. The inaccuracy in the displacement predic-

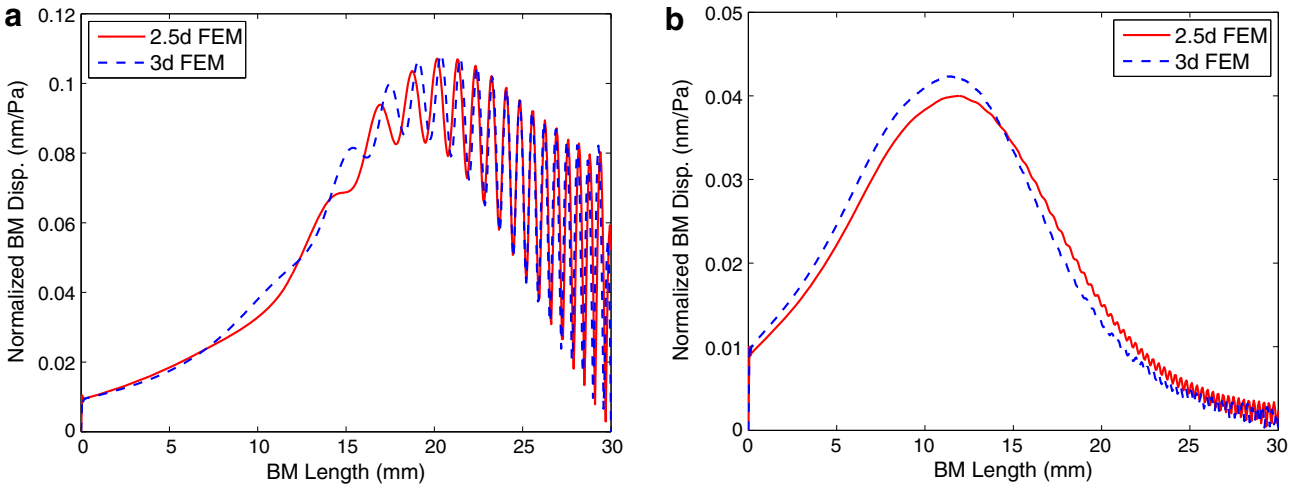

Fig. 10. The comparison of the structure displacement calculated from 2.5D FEM model and 3D FEM model using 27/4 u/p fluid element and Hinton–Huang's structural element: (a) response at 12 kHz; (b) response at 35 kHz. Fluid is inviscid, and pure tensioned membrane model is used for the structure with structural damping $\eta = 0.05$.

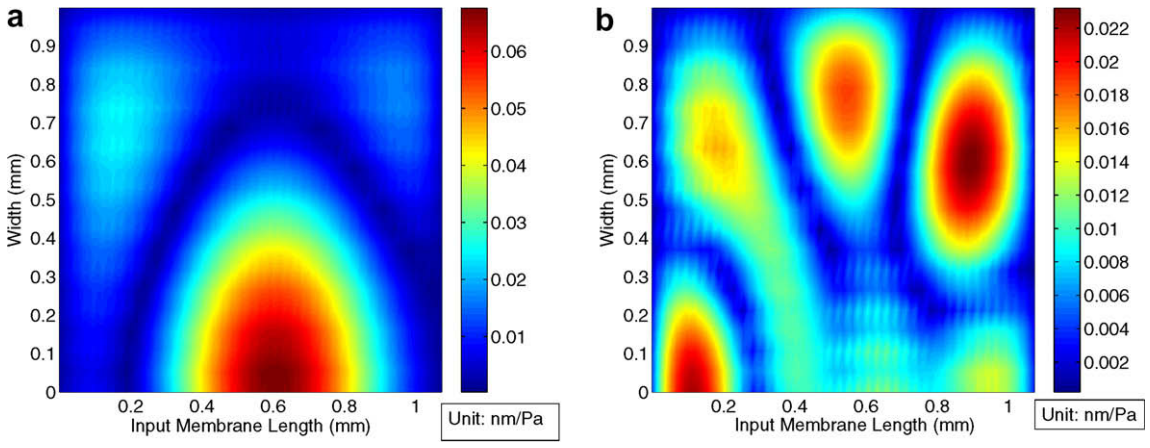

Fig. 11. The two-dimensional view of the displacement of the input membrane calculated from 3D FEM model: (a) response at 12 kHz; (b) response at 35 kHz.

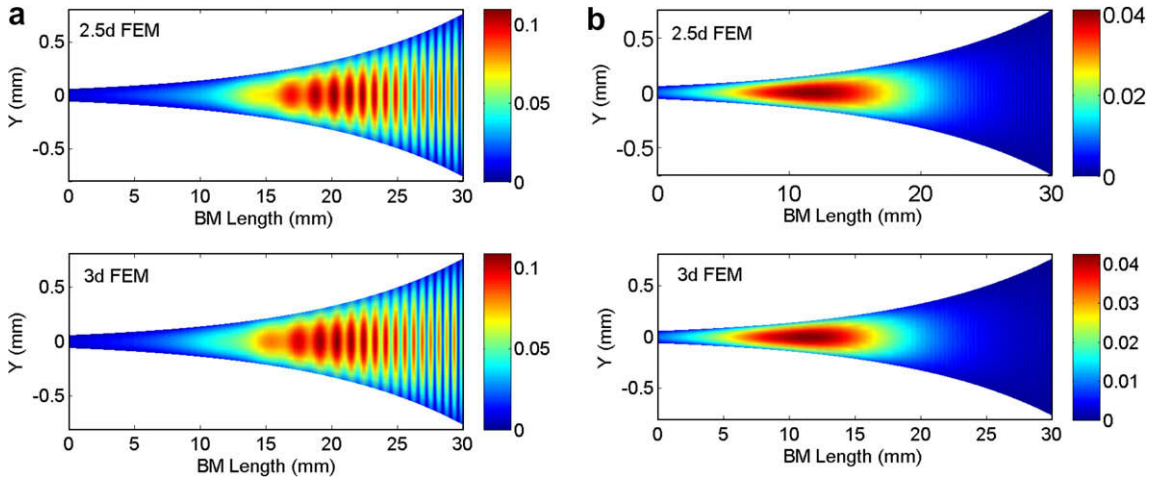

Fig. 12. The two-dimensional view of the BM displacement calculated from 2.5D FEM model and 3D FEM model: (a) response at 12 kHz; (b) response at 35 kHz.

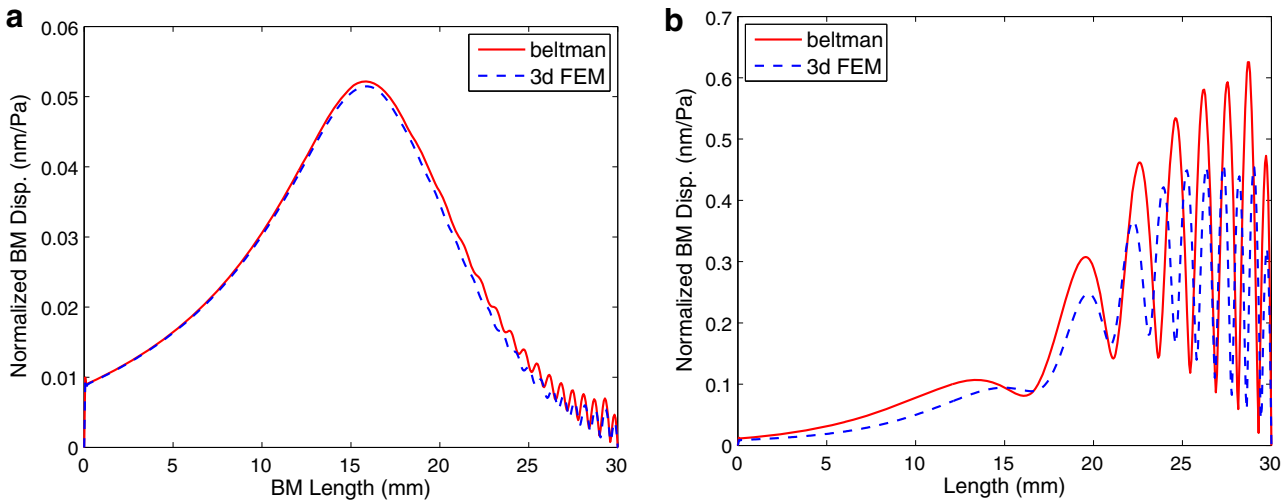

Fig. 13. The comparison of the structure displacement between Beltman's FEM model and 3D FEM model using 27/4 u/p fluid element and Hinton–Huang's structural element at 12 kHz: (a) duct height is 110 μm; (b) duct height is 475 μm. In Beltman's FEM model, 501 × 7 uniform grid is used for plate. In 3D FEM, 501 × 7 uniform grid is used for the plate, and 603 x nodes, 15 y nodes and 21 z nodes are used for the fluid.

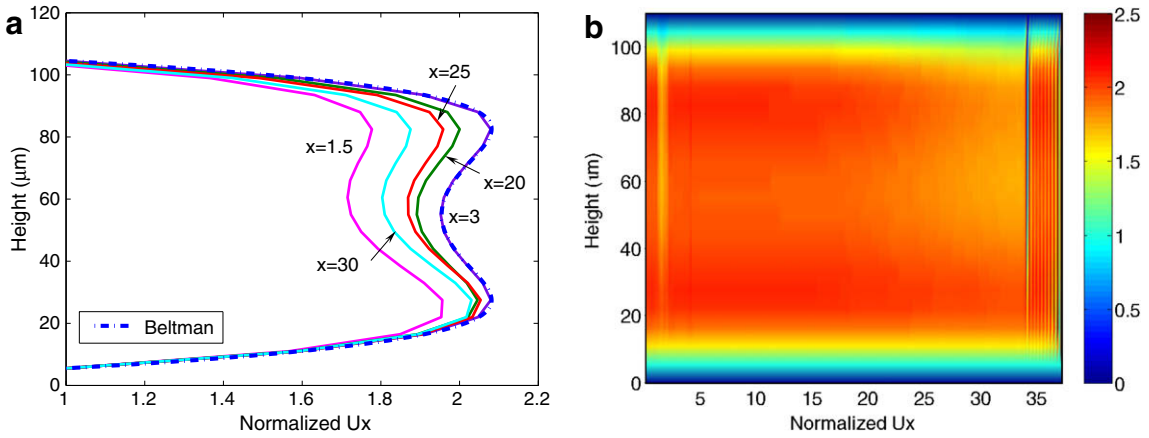

Fig. 14. (a) The comparison of the normalized u_x as a function of x and z at the $y = 0$ plane between Beltman's model and the 3D FEM model for 110 μm-high duct. u_x is normalized at $z = 5.5$ μm. $\mu = 5$ cSt and $f = 12$ kHz. Beltman's model assume that the change of the normalized u_x in the height direction does not vary in x, therefore there is only one curve (dashed line) shown in the figure. The 3D FEM results (solid line) show there are some variation in x, but the variation is small in this case. (b) The two-dimensional view of the normalized u_x as a function of x and z at the $y = 0$ plane in the 3D FEM model.

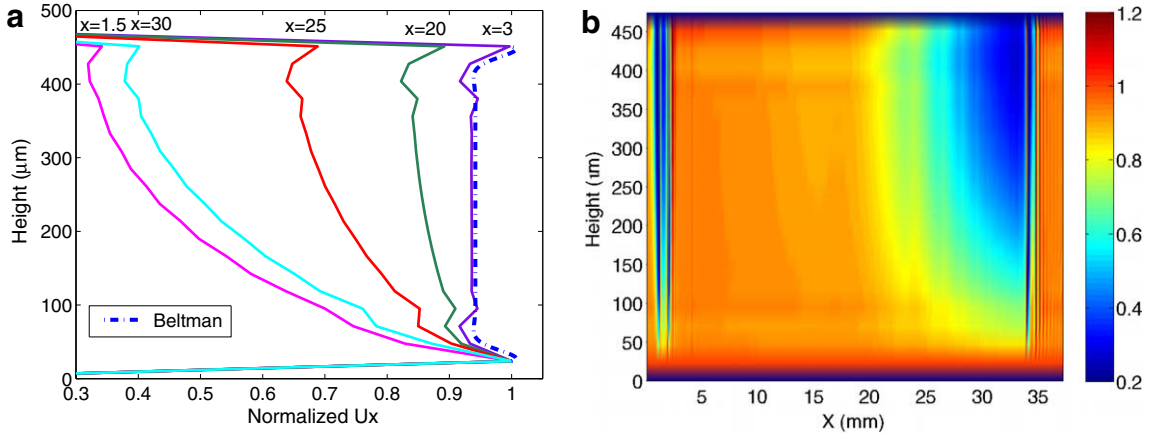

Fig. 15. (a) The comparison of the normalized u_x as a function of x and z at the $y = 0$ plane between Beltman's model and the 3D FEM model using 27/4 u/p fluid element and Hinton–Huang's structural element for 475 μm-high duct. $\mu = 5$ cSt and $f = 12$ kHz. u_x is normalized at $z = 23.75$ μm. Beltman's model assume that the change of the normalized u_x in the height direction does not vary in x, therefore there is only one curve (dashed line) shown in the figure. The 3D FEM results (solid line) show the variation of the u_x curves is large at some locations from dashed line. (b) The two-dimensional view of the normalized u_x as a function of x and z at the $y = 0$ plane in the 3D FEM model.

tion could be a result of the thin-film assumption, which may be violated for the larger-height duct model.

To examine this question, we can compare the fluid displacements in the x or y directions in the $y = 0$ plane between the 3D model and the thin film model. Based on Beltman's assumption, in the fluid domain the thin film model requires,

$$u_x = -\frac{1}{\rho_f i w}\frac{\partial P}{\partial x}A(z), \tag{39}$$

where the function $A(z)$ does not depend on x. The function $A(z)$ describes the variation of the normalized u_x in the height direction regardless of the x locations. Fig. 14a shows the comparison of the normalized u_x as a function of the height at 12 kHz between Beltman's model and the 3D FEM model at the $y = 0$ plane. Note here the displacement u_x is normalized to the first non-zero displacement point from the boundary $z = 0$ at each x location. At 12 kHz, the u_x in the 3D FEM model does not exactly follow the curve for the Beltman's model (dashed line) at different x locations, but the variation is small. However at 35 kHz, the u_x curve is very different from the dashed line, especially in the region left of the BM ($x < 3$ mm) and some portion in the BM (20 mm $< x <$ 35 mm). Figs. 14b and 15b give a two-dimensional view of the normalized u_x as a function of the height and x location at 12 kHz and 35 kHz, respectively. The in-plane displacement goes to zero at the top and bottom boundaries as we defined in the boundary condition. Fig. 14a can be obtained by taking the slice cuts at different x locations in Fig. 14b.

Another advantage of the full 3D FEM model is that it can model irregular geometries, while all the other cochlear models including WKB model [16] and other FEM models described here have certain limitations on the geometries. The WKB model requires that the input to the system must be located at the wall $x = 0$ and the geometry of the duct is rectangular (the duct height could be slowly varying [16]). The 2.5D model uses the modal solution in the y direction and does not allow any abrupt variation in the width of the duct. Beltman's model assumes a constant pressure in the height direction, thus when some portion of the duct height changes, we may need to break the fluid domain into constant height regions and apply continuity conditions at the interface. Since the variation in the duct height or width may not be avoidable in the device, having a FEM model which can deal with arbitrary 3D geometry is useful.

A second model case will now be presented for a hydromechanical cochlear model with a more irregular geometry. The geometry and the dimension of the model are given in Fig. 16 and described in more detail elsewhere [26]. The duct is taller (0.475 mm) at the places where the input membrane and the BM are located and shallower (0.275 mm) elsewhere. The membranes are isotropic,

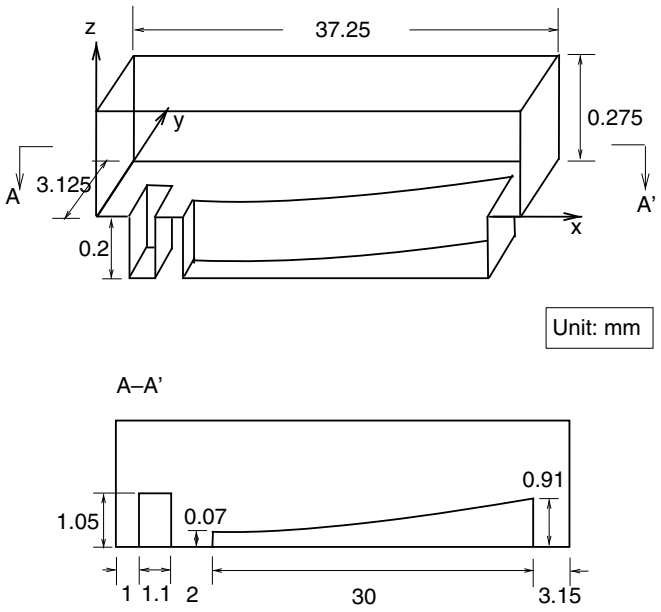

Fig. 16. The dimension of the duct and the structure. The thickness of the structure is 0.32 μm

Table 2
Material properties for the example problem

Symbols	Value	Unit	Physical meaning
ρ_f	950	kg/m^3	Fluid density
c	1000	m/s	Fluid wave speed
μ	200/20	cSt	Fluid viscosity
ρ_p	2.9×10^{-3}	kg/m^2	Plate area density
E_x	160	GPa	Young's modulus in x
E_y	160	GPa	Young's modulus in y
ν	0.23		Poisson's ratio
T_x	50	N/m	Tension in x
T_y	50	N/m	Tension in y

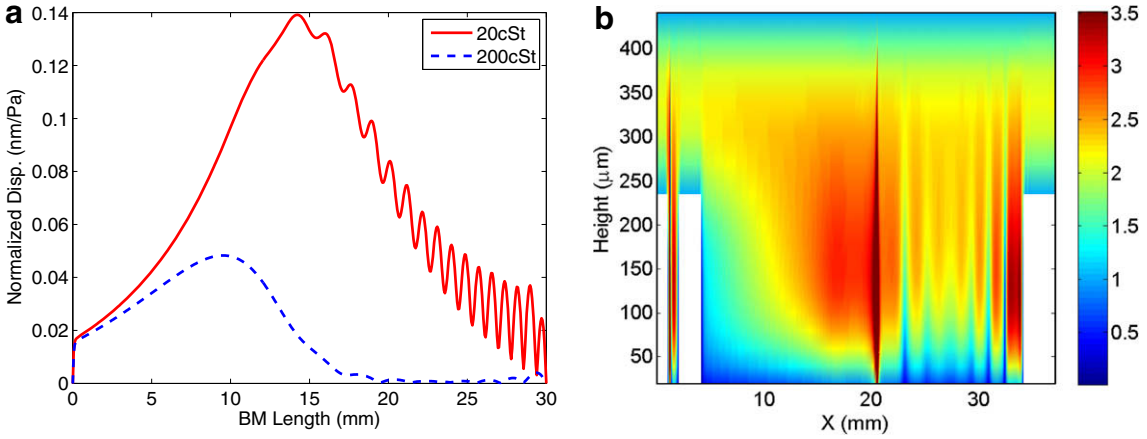

Fig. 17. (a) The structural displacement at 10 kHz for two different viscosities: 200 cSt and 20 cSt. (b) The profile of the normalized u_x as a function of x and z at $y = 0$ plane. The computation was done at 10 kHz for 200 cSt fluid.

and made from a laminate of silicon nitride/doped polysilicon/silicon nitride (0.1 μm/1 μm/0.1 μm). The structure is still micromachined from silicon and glass and anodically bonded together. Silicone oil is still used as the fluid medium. The estimated material properties for the device are given in Table 2. Fig. 17a shows the computed BM displacement at 10 kHz for two different viscosities: $\mu = 200$ cSt and $\mu = 20$ cSt. The BM displacement exhibits steeper cut-off after the resonance peak for the higher viscosity, but the magnitude is smaller (10 dB lower compared to 20 cSt case). In addition, the resonant peak appears more towards the narrow end of the BM.

The normalized fluid displacement u_x as a function of x and the height at $y = 0$ plane is shown in Fig. 17b. The calculation was performed using 200 cSt fluid at 10 kHz. For an irregular geometry like this, it is clear that Beltman's model can no longer be applied in the whole domain due to the variation in the height at different x locations. The normalized u_x shows a uniform profile along the height direction in the regions where there are no membranes present (smaller height regions in the figure). However, in the regions where the duct is deeper, there is significant variation in the profile of the normalized u_x. Thus Beltman's thin film formulation will no longer be a good approximation.

6. Summary

In this paper, a full three-dimensional FEM model is introduced for fluid–structure interaction systems including but not limited to the cochlea or cochlear-based transducers. The Hinton–Huang's formulation to discretize the structure can be used to model a pure tensioned membrane or a pure bending plate or both. Note that two rotational degrees of freedom (θ_x and θ_y) need to be set zero at each structural node for a pure tensioned membrane model since the membrane model only has one degree of freedom (w). The fluid element has three degrees of freedom per node: the fluid displacements at x, y and z directions. The coupling at the fluid–structure interface is set such that the in-plane displacements are negligible and the out-of-plane displacement is continuous. As a future work, we can also couple two structure rotational degrees of freedom to the fluid in-plane displacements at the interface in order to fully investigate the viscous boundary layer effect. Clearly this FEM model with a three-dimensional discretization and average three degrees of freedom per node has very high computational cost, however, it provides a benchmark solution against which the accuracy of other approximation methods such as Beltman's FEM model [2,25] and 2.5D FEM model [21] can be assessed and it can be used to model the fluid–structure interaction systems when other FEM formulations are not applicable.

References

[1] K.J. Bathe, Formulation of the Finite Element Method – Linear Analysis in Solid and Structural Mechanics, Prentice-Hall, 1996.
[2] W.M. Beltman, P.J.M. Van der Hoogt, R.M.E.J. Spiering, H. Tijdeman, Implementation and experimental validation of a new viscothermal acoustic finite element for acousto-elastic problems, J. Sound Vib. 216 (1) (1998) 159–185.
[3] R.B. Beyer, A computational model of the cochlea using the immersed boundary method, J. Comput. Phys. 98 (1992) 145–162.
[4] F. Böhnke, W. Arnold, 3D-finite element model of the human cochlea including fluid–structure couplings, ORL 61 (1999) 305–310.
[5] R. Bossart, N. Joly, M. Bruneau, Hybrid numerical and analytical solutions for acoustic boundary problems in thermo-viscous fluids, J. Sound Vib. 263 (1) (2003) 69–84.
[6] P. Dallos, A. Popper, R. Fay, The Cochlea, Springer-Verlag, New York, 1996.
[7] G.C. Everstine, A symmetric potential formulation for fluid–structure interaction, J. Sound Vib. 79 (1) (1981) 157–160.
[8] C.A. Figueroa, I.E. Vignon-Clementel, K.E. Jansen, T.J.R. Hughes, C.A. Taylor, A coupled momentum method for modeling blood flow in three-dimensional deformable arteries, Comput. Methods Appl. Mech. Engrg. 195 (41–43) (2006) 5685–5706.
[9] R.Z. Gan, B.P. Reeves, X. Wang, Modeling of sound transmission from ear canal to cochlea, Ann. Biomed. Engrg. 35 (12) (2007) 2180–2195.
[10] E. Givelberg, J. Bunn, A comprehensive three-dimensional model of the cochlea, J. Comput. Phys. 191 (2003) 377–391.
[11] M.A. Hamdi, Y. Ousset, G. Verchery, A displacement method for analysis of vibrations of coupled fluid–structure systems, Int. J. Numer. Methods Engrg. 13 (1) (1978) 139–150.
[12] E. Hinton, H.C. Huang, A family of quadrilateral Mindlin plate elements with substitute shear strain fields, Comput. Struct. 23 (3) (1986) 409–431.
[13] M.H. Holmes, J.D. Cole, Cochlear mechanics: analysis for a pure tone, J. Acoust. Soc. Am. 76 (1984) 767–778.
[14] T.J.R. Hughes, In the Finite Element Method, Dover Publications, Inc., 1987, (Chapter 4).
[15] L. Kiefling, G.C. Feng, Fluid–structure finite-element vibrational analysis, AIAA J. 14 (2) (1976) 199–203.
[16] K.M. Lim, Physical and Mathematical Cochlear Models, Ph.D. Thesis, Stanford University, 2000.
[17] K.M. Lim, C.R. Steele, A three-dimensional nonlinear active cochlear model analyzed by the WKB-numeric method, Hear. Res. 170 (1–2) (2002) 190–205.
[18] H. Morand, R. Ohayon, Substructure variational analysis of the vibrations of coupled fluid structure systems – finite-element results, Int. J. Numer. Methods Engrg. 14 (5) (1979) 741–755.
[19] L.G. Olson, K.J. Bathe, A study of displacement-based finite elements for calculating frequencies of fluid and fluid–structure systems, Nucl. Engrg. Des. 76 (1983) 137–151.
[20] E. Onate, O.C. Zienkiewicz, B. Suarez, R.L. Taylor, A general methodology for deriving shear constrained Reissner–Mindlin plate elements, Int. J. Numer. Methods Engrg. 33 (2) (1992) 345–367.
[21] A.A. Parthasarathi, K. Grosh, A.L. Nuttall, Three-dimensional numerical modeling for global cochlear dynamics, J. Acoust. Soc. Am. 107 (2000) 474–485.

[22] C.R. Steele, L.A. Taber, Comparison of WKB calculations and experimental results for three-dimensional cochlear models, J. Acoust. Soc. Am. 65 (1979) 1007–1018.
[23] X.D. Wang, K.J. Bathe, Displacement pressure based mixed finite element formulations for acoustic fluid–structure interaction problems, Int. J. Numer. Methods Engrg. 40 (11) (1997) 2001–2017.
[24] L. Watts, The mode-coupling Liouville–Green approximation for a two-dimensional cochlear model, J. Acoust. Soc. Am. 108 (5) (2000) 2266–2271.
[25] R.D. White, K. Grosh, Microengineered hydromechanical cochlear model, Proc. Natl. Acad. Sci. USA 102 (5) (2005) 1296–1301.
[26] R.D. White, R. Littrell, K. Grosh, Copying the cochlea, micromachined biomimetic acoustic sensors, in: Fu-Kuo Chang (Ed.), Structural Health Monitoring 2007, Quantification, Validation and Implementation, DesTECH Publications, Inc., 2007, pp. 1447–1454. volume 2 edition.